

Mixing at the head of a canyon: A laboratory investigation of fluid exchanges in a rotating, stratified basin

Judith R. Wells^{1,2} and Karl R. Helfrich¹

Received 25 April 2006; revised 18 July 2006; accepted 3 August 2006; published 5 December 2006.

[1] Observations indicate that oceanic mixing is intensified near the head of submarine canyons. How the presence of canyon walls affects the local production and distribution of mixed fluid is an open question. These dynamics are addressed through rotating tank experiments which impose mixing at middepth at the closed end of a channel open to a larger body of water. Turbulence is generated in a linearly stratified fluid with initial buoyancy frequency N by means of a single bar oscillated with frequency ω . The mixed fluid quickly reaches a steady state height $h \sim (\omega/N)^{1/2}$ independent of the Coriolis frequency f and collapses into the channel interior. A small percentage of the fluid exported from the turbulent zone enters a boundary current. The bulk forms a cyclonic circulation in front of the bar. As the recirculation cell expands to fill the channel, it restricts horizontal entrainment into the turbulent zone. Mixed fluid flux decays with time as $t^{-1/2}$ and is dependent on the size of the mixing zone and the balance between turbulence, rotation, and stratification. The recirculation cell is confined within the channel, and export of mixed fluid into the basin is restricted to the weak boundary current. As horizontal entrainment is shut down, long-term production of mixed fluid relies more on vertical entrainment. However, the scalings indicate that short-term dynamics are the most applicable to oceanic conditions.

Citation: Wells, J. R., and K. R. Helfrich (2006), Mixing at the head of a canyon: A laboratory investigation of fluid exchanges in a rotating, stratified basin, *J. Geophys. Res.*, *111*, C12004, doi:10.1029/2006JC003667.

1. Introduction

[2] Submarine canyons are dynamically active regions with enhanced turbulence and mixing relative to the open ocean. Off the east and west coasts of North America, vigorously turbulent boundary layers, convergent flows and intrusions of mixed water have been observed at the heads of shelfbreak canyons [Lueck and Osborn, 1985; Gardner, 1989; Carter and Gregg, 2002; Kunze et al., 2002]. Intensified mixing has also been observed over the MidAtlantic Ridge [Polzin et al., 1997; Ledwell et al., 2000] with the highest mixing rates found in transverse fracture zones [St. Laurent et al., 2001]. Shelfbreak canyons and abyssal fracture zones are widespread oceanic features. For example, bathymetric maps show 20 to 30 fracture zones along the MidAtlantic Ridge in the Brazil Basin [St. Laurent et al., 2001]; more than two dozen major canyons cut into Atlantic shelf off the United States [Hunkins, 1988]; and 20% of the Pacific shelf between Alaska and the equator is interrupted by steep narrow canyons [Hickey, 1995].

[3] If the fluid mixed in coastal and abyssal canyons were exported into the open ocean, it could be a significant factor

in setting the basin-scale thermohaline structure and a major contributor to closing global ocean heat and mass budgets [Munk and Wunsch, 1998]. The transport of vertically mixed heat, salinity, chemicals and nutrients could shape the ecology of continental margins. However, if turbulence within canyons merely stirred up already mixed waters it would have little impact. This study seeks to understand the interaction of a laterally confined patch of mixing with the ambient water, and the processes of exchange between a canyon or channel and the open ocean. These objectives are addressed through a laboratory study where aspects of the dynamics are isolated and explored in a simplified setting.

[4] In the experiments presented here, mixing is imposed at the closed end of a channel that opens into a larger basin. The experiments are conducted in a rotating tank filled with linearly stratified salt water. Turbulence is induced by a single oscillating bar of finite width, placed at middepth along a section of the tank perimeter and enclosed on two sides by walls that extend into the tank interior as shown in Figure 1. The experiments investigate the horizontal and vertical entrainment of ambient fluid into the turbulent zone, the export of mixed fluid into the channel, mixed fluid properties, volume and distribution, and exchanges between the channel and the basin. These characteristics are described and quantified as functions of the Coriolis frequency,

¹Woods Hole Oceanographic Institution, Woods Hole, Massachusetts, USA.

²Now at Department of Ocean and Resources Engineering, University of Hawaii at Manoa, Honolulu, Hawaii, USA.

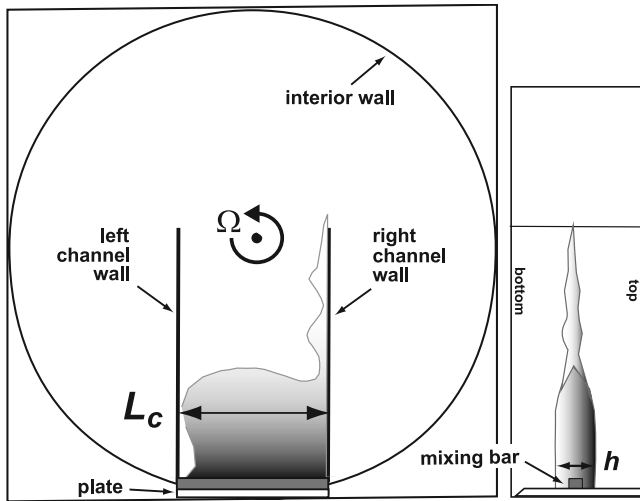


Figure 1. Experimental apparatus with a channel of width L_c . Sketch shows a top view of the 114×114 cm square glass tank, the circular interior wall, the channel walls, and the mixing bar and support plate. To the right of the tank is a 45° mirror giving a side view of the bar. The sketch shows a region of mixed fluid in front of the bar and a boundary current along the right channel wall. Area measurements are made from the top view. The height h is measured from the mirror view at the site of the double-headed arrow.

where Ω is the tank rotation rate about the vertical z axis, and the buoyancy frequency, N ,

$$N^2 = -\frac{g}{\rho_o} \frac{\partial \rho}{\partial z}, \quad (2)$$

where g is the acceleration due to gravity, ρ_o is the reference density, and $\rho(z)$ is the ambient density. Turbulent properties are described as a function of the bar oscillation frequency, ω .

[5] In an earlier laboratory study, Wells and Helfrich [2004], hereinafter referred to as WH04, investigated the effects of an isolated patch of mixing at a vertical boundary in a rotating stratified system. In those experiments the face and both ends of the mixing bar were exposed to the surrounding water. The bar-induced turbulence formed a region of mixed fluid which quickly reached a steady state height and collapsed into the interior. Surprisingly, the mixed fluid did not form a boundary current. Instead, a single intrusion of uniform thickness and finite width moved directly into the interior of the tank with a speed comparable to a gravity current. The flow exiting the turbulent region appeared to be constrained by entrainment-driven horizontal flows approaching the sides of the region. The results indicated that, once the turbulent zone had been established, horizontal rather than vertical entrainment determined both the production rate and pathways of mixed fluid. The striking flow patterns raised questions about the relationship of lateral access to the mixing region and the mixing dynamics. Would channel walls at the sides of mixing bar block horizontal entrainment and reduce the production of mixed fluid? Would a reduction in horizontal inflow encourage vertical entrainment, increase the thickness of the mixed layer or promote its continued growth?

Would the presence of sidewalls promote boundary current formation and redirect flow in the interior of the tank?

[6] The channel experiments, described here, use a laboratory configuration identical to the WH04 setup except for the addition of the two channel walls. The experiments are conducted with an equivalent range of bar widths and variation in Coriolis and buoyancy frequencies. Section 2 describes the laboratory apparatus and measurement methods, and outlines the parameterization of bar-induced turbulence developed in WH04. Section 3 summarizes the results of the earlier experiments in order to allow a comparison between mixing by exposed and laterally confined turbulent patches. Section 4 presents a qualitative description of the distribution of mixed fluid, and section 5 provides a quantitative analysis of the production of mixed fluid and its partition between a recirculation cell and a boundary current. In section 6 geostrophic transports are calculated from cross-channel density profiles and the three-dimensional flow field is inferred. Section 7 investigates the limits of rotational effects on mixed fluid flux. The concluding section summarizes the laboratory results and examines their application to oceanic mixing.

2. Experimental Design

2.1. Laboratory Apparatus and Measurement Techniques

[7] A sketch of the laboratory apparatus is given in Figure 1. The 114×114 cm² glass tank was fitted with an interior circular Plexiglas wall forming a cylindrical working section that prevented corner effects from complicating interior flows. The adjacent 45° mirror provided a side view for a video camera mounted five meters above the tank. The tank and mirror were placed on a two meter diameter turntable, and both table and camera rotated with angular frequency $\Omega = f/2$ (counterclockwise when viewed from above). The tank was filled with linearly stratified salt water to a working depth of 26 cm.

[8] Turbulent mixing was produced by a vertically oscillating single horizontal bar with a fixed cross section, 1.27×1.27 cm², and a variable length, [20.3, 25.4, 30.5 cm]. The motion was sinusoidal with amplitude, $A = 0.35$ cm, and frequency, $\omega = 14$ s⁻¹. Figure 1 shows the bar mounted at middepth on a support plate which was set into a flat section of the interior wall. Two 61 cm-long Plexiglas walls abutted the sides of the mixing bar and extended the full depth of the fluid. The outer wall and sidewalls enclosed the mixing bar on three sides, creating a channel which opened into the center of the basin. A rigid lid, placed over the interior framework, eliminated surface waves generated by the vertical motion of the mixer.

[9] Linear stratification was accomplished through the two-reservoir method [Oster, 1965]. Increasingly dense water was introduced over a two hour period into the bottom of the rotating tank through a diffuser covered by a layer of sand. The fluid continued to spin up for an additional twelve hours. Prior to the initiation of mixing, the background velocity field was checked. Velocities were $O(10^{-3}$ cm s⁻¹), negligible with respect to the mixing-induced circulations, and the vertical structure and horizontal direction of the flow showed no distinct pattern.

[10] Data on the production and circulation of mixed fluid were acquired through visual images of dye distributions and from density profiles made with a Precision Measurement Engineering conductivity probe. The WH04 experiments showed a tight correspondence between dye image and probe profile measurements, validating the use of dye as a marker for mixed fluid. In the present experiments a syringe pump slowly injected neutrally buoyant dye at three points along the mixing site. The dye was quickly dispersed and moved with the mixed fluid. The overhead camera photographed the top and reflected side views of the spreading dye, and the images were recorded both on video tape and in directly digitized computer sequences at known time intervals. Figure 1 sketches a typical dye distribution with recirculating fluid in front of the bar and a boundary current along the right-hand channel wall. The images are used to measure mixed layer height, area and volume, to evaluate the partition of mixed fluid between the recirculation zone and the boundary current, and to describe the pathways of entrainment and export.

[11] The conductivity probe recorded the initial buoyancy frequency N of each experiment. For selected experiments, series of closely spaced vertical density profiles were made across the channel through the center of the recirculation region. The transects provide a picture of both the vertical and horizontal density distributions. This information is used in section 5.2 to assess cross-channel variations in mixed layer height. In section 6, the horizontal density differences are used to calculate geostrophic velocities and infer circulation within the channel.

[12] The primary independent variables, N and f , were varied over the ranges $N = [0.3, 0.6, 0.9]\text{s}^{-1}$, and $f = [0, 0.1, 0.2, 0.3, 0.6, 0.9, 1.2]\text{s}^{-1}$. The bar frequency was fixed at $\omega = 14\text{ s}^{-1}$ with $\frac{\omega}{N}, \frac{\omega}{f} \gg 1$, so that bar motion would create localized turbulent mixing rather than internal or inertial waves. The main set of dye injection experiments was conducted with a channel width L_C corresponding to the maximum mixing bar length, $L_C = 30.5\text{ cm}$. After the results of the rotating and nonrotating experiments were analyzed for $L_C = 30.5\text{ cm}$, the role of channel width was investigated in experiments with $L_C = [25.4, 20.3]\text{cm}$. The cross-channel probe transects were undertaken in four separate experiments, with $N = [0.3, 0.9]\text{s}^{-1}$, $f = [0.1, 0.3, 1.2]\text{s}^{-1}$ and $L_C = 30.5\text{ cm}$.

2.2. Parameterization of Bar-Induced Turbulence

[13] The parameterization of bar-induced turbulence, described in detail by WH04, follows from the *Hopfinger and Toly* [1976] model of the spatial decay of turbulence and from similar experimental studies of the inhibition of turbulence by buoyancy. *Hopfinger and Toly* [1976] generated turbulence through vertical oscillation of a horizontally planar grid of intersecting bars. Direct measurements of the r.m.s. velocity, u_t , and the integral length scale, l_t , established that grid motion produced nearly isotropic turbulence, and that the turbulent length scale increased with distance d from the grid,

$$l_t = \beta d, \quad (3)$$

where β was an empirically determined constant, while turbulent velocity decreased inversely with distance, $u_t \sim d^{-1}$.

The turbulent velocities were dependent on the grid geometry, and the frequency ω and amplitude A of grid oscillation.

[14] In the WH04 parameterization of bar-induced turbulence, turbulent velocity u_t is represented by

$$u_t = G \frac{\omega}{d}, \quad (4)$$

where G incorporates bar cross-sectional geometry and stroke amplitude and has the dimensions of length squared. The quantity of interest in the derivation of length scales for analyzing the mixing experiments is the inverse of the turbulent timescale (l_t/u_t) $^{-1}$. From equations (3) and (4) this term is written as

$$u_t/l_t = \gamma^2 \frac{\omega}{d^2}, \quad (5)$$

where $\gamma \equiv (\frac{G}{\beta})^{1/2}$ and has units of cm. The constant γ was determined through a series of laboratory experiments (WH04) and found to be $\gamma = 0.98\text{ cm}$. This value is specific to the single bar mixing mechanism with the fixed stroke amplitude used in both the WH04 and the present experiments.

2.3. Experimental Length Scales

[15] The length scales used in evaluating the channel mixing experiments include the width of the mixing region, given by the channel width/bar length L_O , and three other scales constructed from the frequencies N , f and ω . Two follow from the assumption that motion at the interface of the turbulent zone and the ambient rotating stratified fluid is set by a balance between the intrinsic timescale of the turbulence, l_t/u_t , and the buoyancy and rotation periods, N^{-1} and f^{-1} .

[16] When turbulence occurs in stably stratified fluids, buoyancy forces tend to inhibit vertical motion [Linden, 1973; Turner, 1973; Fernando, 1988; Fleury *et al.*, 1991]. The Ozmidov [1965] length scale,

$$L_O = \left(\frac{\varepsilon}{N^3} \right)^{1/2}, \quad (6)$$

arises from the balance of buoyancy and inertial forces. The dissipation rate of turbulent kinetic energy ε is given by

$$\varepsilon = \frac{u_t^3}{l_t}. \quad (7)$$

Stratification has little effect on turbulence with length scales $l_t < L_O$. However, as l_t approaches L_O , buoyancy suppresses turbulence and overturning eddies reach their maximum vertical scale (i.e., $l_t \sim L_O$). This limit corresponds to an internal turbulent Froude number,

$$Fr_t \equiv \frac{u_t}{N l_t}, \quad (8)$$

of order one.

[17] Laboratory studies have also demonstrated that rotation imposes similar constraints on three-dimensional tur-

bulence [Dickinson and Long, 1983; Hopfinger *et al.*, 1982]. The analogy with stratified flow suggests that turbulent motions sufficiently close to an oscillating grid will behave independently of rotation. At a critical distance from the grid, rotation will suppress the vertical turbulent motion. This transition is expected when the turbulent Rossby number,

$$Ro_t \equiv \frac{u_t}{f l_t}, \quad (9)$$

approaches unity from above.

[18] The distances from the bar at which the turbulent Froude (equation (8)) and Rossby (equation (9)) numbers equal unity can be found using the bar parameterization for l_t/u_t (equation (5)). A buoyancy height scale and rotational length scale are determined by the critical distances for the suppression of isotropic turbulence by stratification and rotation, respectively. The buoyancy height scale is defined as

$$H_N \equiv \gamma \left(\frac{\omega}{N} \right)^{1/2}. \quad (10)$$

and the rotational length scale, L_f , is

$$L_f \equiv \gamma \left(\frac{\omega}{f} \right)^{1/2}. \quad (11)$$

[19] The third length scale used in analyzing the experimental results is the internal Rossby radius of deformation, hereafter referred to as the deformation radius, based on a vertical height h ($\sim H_N$),

$$L_R = \frac{Nh}{f}. \quad (12)$$

The deformation radius is the horizontal scale at which rotation begins to control the outflow. The experimental values of N , f and ω give $4 \leq H_N \leq 7$ cm, $3 \leq L_f \leq 12$ cm and $2 \leq L_R \leq 35$ cm.

[20] Figure 2 is a regime diagram of the experiments. Each experiment is characterized by two nondimensional numbers: the ratio of the buoyancy to the Coriolis frequency N/f , and the parameter L_C/L_R which compares channel width to the distance within which the flow will feel the effects of rotation. The dye injection experiments cover the parameter ranges, $\frac{1}{4} \leq N/f \leq 9$ and $1 \leq L_C/L_R \leq 18$. The four experiments performed with cross-channel transects span the same parameter range, with $N/f = [\frac{1}{4}, 1, 3, 9]$ and $L_C/L_R = [18, 4.7, 3, 1]$. They are indicated by diamonds on the regime diagram.

3. Unconfined Localized Mixing: Experimental Results

[21] The WH04 experiments were designed to investigate the production and distribution of mixed fluid associated with an isolated patch of boundary mixing, where the patch was exposed to vertical entrainment from above and below and to horizontal entrainment on three sides. The experimental setup

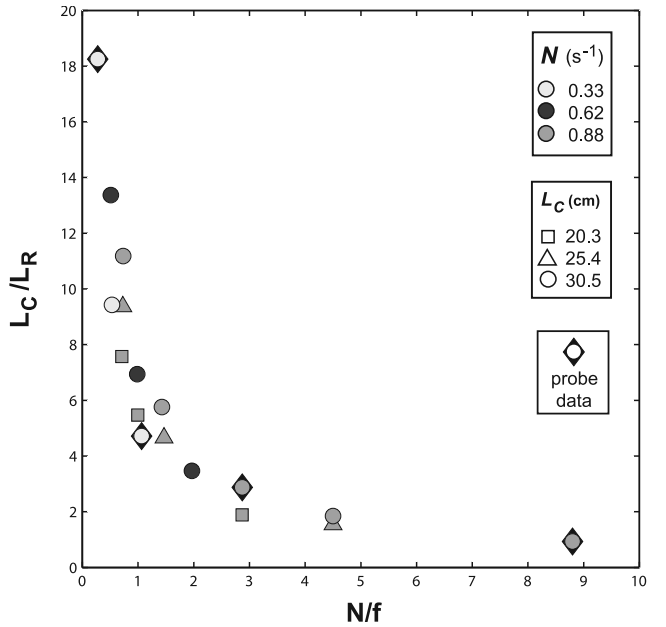


Figure 2. Regime diagram. Each experiment is shown with respect to N/f , the ratio of buoyancy and Coriolis frequencies, and L_C/L_R , the ratio of channel width to the deformation radius (equation (12)). The symbols indicate initial buoyancy frequency and channel width. The diamonds designate the probe experiments.

was exactly as described in section 2.1 except that there were no walls blocking the sides of the bar. The results of these unconfined experiments are summarized below for comparison with results from the channel experiments.

[22] Observations of the flow indicated that the mixing generated by the single oscillating bar was fed by lateral entrainment of ambient fluid along the walls of the tank. The mixed fluid was exported in a layer of uniform height directly into the tank interior. Mixed layer height was found to be a function of stratification and independent of rotation. WH04 found (cf. equation (10))

$$h_m = (0.97 \pm 0.05) \gamma \left(\frac{\omega}{N} \right)^{1/2}, \quad (13)$$

where $\gamma = 0.98$ cm. The horizontal area of mixed fluid A_m scaled with both the rotational length scale L_f (equation (11)) and the deformation radius L_R (equation (12)), suggesting that lateral spreading of mixed fluid was more than a laminar adjustment of the flow to background rotation. The scaling implied that the characteristics of the mixed layer were determined, in part, by the rotational control of turbulent motion. WH04 found

$$A_m = (0.15 \pm 0.03) L_R L_f f t. \quad (14)$$

The volume of mixed fluid, $V_m = A_m h_m$, grew linearly with time producing a constant flux, $dV_m/dt = Q$,

$$Q = 0.16 L_R L_f h_m f. \quad (15)$$

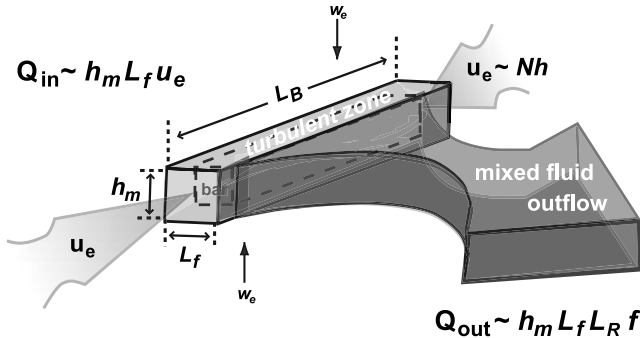


Figure 3. Exposed patch of boundary mixing. Shown is a schematic diagram of the outward flux of mixed fluid and the lateral entrainment of stratified fluid at the sides of the turbulent zone. The dimensions of the turbulent zone are labeled $L_B \times L_f \times h_m$, where L_B is the bar length and L_f and h_m are given by equations (11) and (13), respectively. (See Wells and Helfrich [2004, Figure 13]. Reprinted with the permission of Cambridge University Press.)

[23] WH04 interpreted the volume flux of exported mixed fluid through a model of lateral entrainment. The basic features of the model are illustrated in Figure 3. The model assumed that horizontal entrainment dominated any vertical entrainment and that it occurred at the sides of the mixing zone over the rotational length scale L_f . It further assumed an entrainment velocity, $u_e \sim Nh_m$, consistent with a thermal wind balance in the ambient fluid with length scale L_R . The volume of the actively turbulent zone scaled as $V_t \sim L_B L_f h_m$, where L_B was the bar length.

[24] As sketched in Figure 3, ambient fluid entered across a surface area $h_m L_f$ with a velocity u_e , giving an influx $Q_{in} = h_m L_f u_e$. With negligible vertical entrainment, the mixed fluid outflow had to equal twice this inflow. Thus, with $u_e \sim Nh_m = L_R f$, the efflux was $Q_{out} \sim h_m L_f L_R f$, consistent with the experimental observations (equation (15)). Density was conserved since the inflow was linearly stratified and the outflow vertically well mixed with the mean density. Estimates of vertical entrainment rates supported the assumption that lateral entrainment dominated the production of mixed fluid. Interestingly, the scaling implied that the production of mixed fluid was independent of the mixing zone width, given by the bar length L_B . This conclusion was confirmed through a series of experiments with other bar lengths, $L_B = [15.2, 20.3, 22.9, 30.5]$, $1.8 \leq L_B/L_R \leq 18$.

4. Confined Mixing: Qualitative Description

4.1. Evolution of the Mixed Layer

[25] The typical formation and spreading of fluid mixed at the head of a channel is illustrated in Figure 4 with images from an experiment with $(\omega, N, f) = (14, 0.61, 0.62)\text{s}^{-1}$, $N/f = 1$ and $L_C/L_R = 7$. Turbulent mixing of the stratified fluid begins with the onset of bar oscillation at $t = 0$. Figure 4a, at $t = 70$ s, shows mixed fluid in front of the bar and a developing cyclonic eddy at the base of the boundary current. The eddy grows into a recirculation cell (Figure 4b, $t = 360$ s), which expands to fill the width of the channel and spreads outward from the bar. A distinct boundary current advances along the right-hand wall and

turns the sharp corner at the end of the channel. The current develops regularly spaced, standing lobes which elongate with time. Figure 4e shows a lobe being engulfed by the cyclonic cell of mixed fluid at $t = 1800$ s. By $t = 3600$ s (Figure 4f), a lobe formed by flow separation at the corner of the wall has established a separate pathway to the exterior basin. However, the majority of mixed fluid is still within the channel.

[26] The recirculating region and boundary current are also apparent in the sideview images of the mixed layer. Figure 5 shows images at $t = 40$ s, when the boundary current is just emerging from the mixed region, and at $t = 600$ s, when both features are clearly defined. The recirculating zone is distinguished by its relatively uniform height, while the thinner boundary current tapers toward the nose. The dark, thicker patches on the boundary current are the laterally extended lobes.

4.2. Variations in Flow Patterns

[27] All the rotating, stratified experiments display the same dual structure, a recirculating region spanning the channel in front of the mixing bar and a boundary current following the right-hand wall and exiting the channel. However, within this basic pattern there is considerable

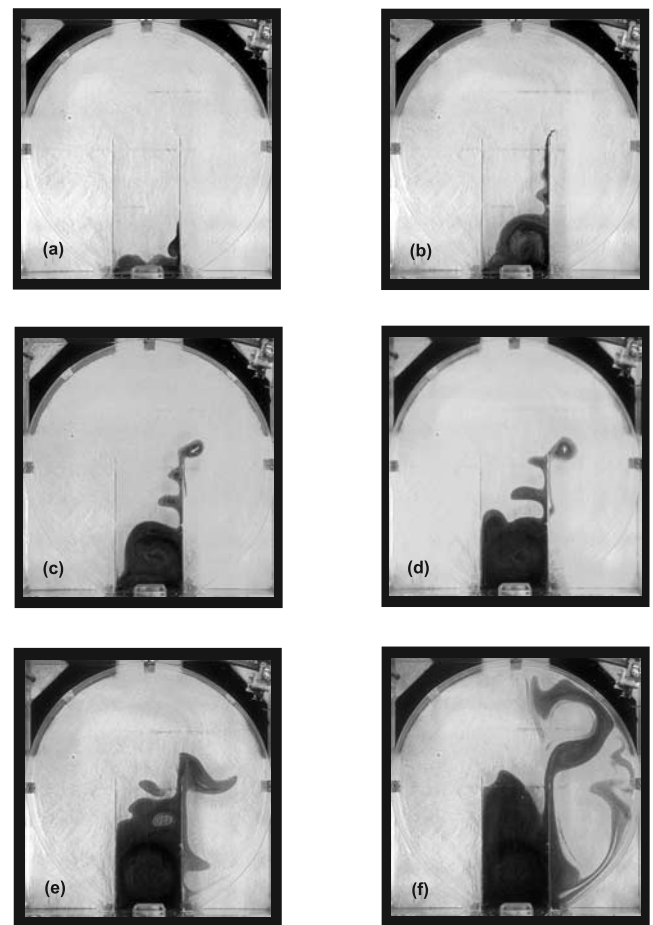


Figure 4. Dye images for an experiment with $(\omega, N, f) = (14, 0.6, 0.6) \text{ s}^{-1}$, $L_C = 30.5 \text{ cm}$, $N/f = 1$, and $L_C/L_R = 7$: (a) $t = 70$ s, (b) $t = 360$ s, (c) $t = 600$ s, (d) $t = 900$ s, (e) $t = 1800$ s, and (f) $t = 3600$ s.

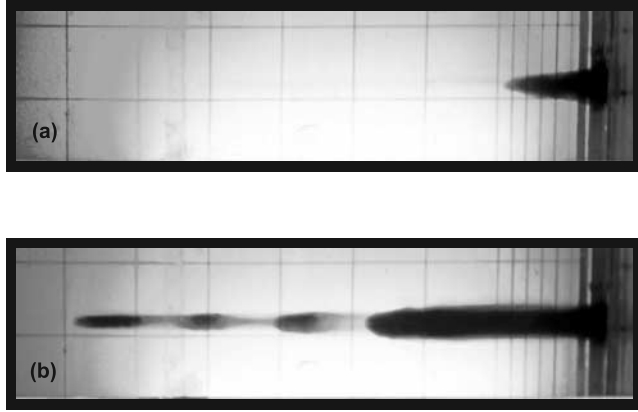


Figure 5. Side view images for an experiment with $(\omega, N, f) = (14, 0.6, 0.6) \text{ s}^{-1}$, $L_C = 30.5 \text{ cm}$, $N/f = 1$, and $L_C/L_R = 7$: (a) $t = 40 \text{ s}$ and (b) $t = 600 \text{ s}$.

variety. Figure 6 shows images taken at $t = 600 \text{ s}$ during three experiments covering a range of values for N/f and L_C/L_R .

[28] The experiment shown in Figure 6a has a low value of $N/f = \frac{1}{2}$ and a correspondingly high value of $L_C/L_R = 15$. The recirculation region has not yet spread across the channel and is still distinct from the mixed fluid emerging from the turbulent zone. The absence of dyed fluid along the left-hand wall suggests a possible avenue for lateral inflow of ambient fluid into the turbulent zone. In Figure 6b, where $N/f = 2$ and $L_C/L_R = 4$, a patch of undyed fluid can be seen to the left of the turbulent zone, but the fully developed recirculation cell spans the channel width and extends halfway down its length. Figure 6c shows the experiment with the highest ratio of stratification to rotation frequencies, with $N/f = 9$ and $L_C/L_R = 1$. The channel is nearly filled with mixed fluid and a wide flow exits the right-hand side of the channel. Only the darker dye in the interior of the channel suggests the presence of both a recirculating cell and boundary current. However, the two structures had been distinct until mixed fluid nearly filled the channel at $t \approx 500 \text{ s}$.

[29] The analysis in section 5 focuses on the production of mixed fluid and relies on measurements of the recirculation region and boundary current taken prior to the appearance of instabilities. The experiments, however, demonstrate numerous examples of lobes and waves forming along the rim of the recirculating cell and at the edge of the boundary current. Earlier laboratory studies of density-driven boundary currents in rotating systems have examined properties of these ageostrophic, wave-like disturbances [Griffiths, 1986]. Experiments with axisymmetric boundary currents [Griffiths and Linden, 1982] showed that, in the case of currents much wider than the deformation radius L_R , disturbances had a length scale proportional to L_R . Otherwise the disturbances scaled with current width. A similar scaling applied when the vertical boundary was omitted, leaving a circular vortex.

[30] In the present experiments baroclinic disturbances develop along the rim of the recirculating cell in experiments where $L_C/L_R > 9$. For a fully developed cell, $\frac{1}{2} L_C$ might be considered the equivalent of the vortex radius. The boundary currents are also characterized by L_C/L_R , but here L_C is simply a length scale associated with the domain and

is unrelated to current width. All the boundary currents in these experiments are much narrower than L_R , but the disturbances nevertheless scale with L_R . The images in Figures 4 and 6 illustrate the changing character of the boundary current as a function of L_C/L_R . In experiments where $L_C/L_R > 5$, multiple disturbances appear on the edge of the boundary current with spacing roughly proportional to L_R . When the disturbance amplitudes are approximately $5 L_R$, they tend to break backward and eventually merge with the recirculation region.

[31] Both the rim and boundary current instabilities distribute mixed fluid further into the channel. However, the horizontal dispersion of mixed fluid within the channel does not directly affect the distribution of mixed fluid in the larger basin. As seen in Figure 4f, the recirculating cells remain within the channel while the boundary current continues as the conduit for mixed fluid leaving the channel.

4.3. Comparison With Mixing in a Closed Channel

[32] The laboratory study of Davies *et al.* [1991] provides an interesting comparison to the present experiments. Their experimental configuration was the equivalent of a closed channel. They used a horizontally oriented, vertically oscillating meshed grid to generate turbulence at the narrow end of a rotating rectangular tank filled with linearly stratified salt water. The grid motion quickly established a mixed layer which collapsed into the tank interior, forming a region of mixed fluid in front of the grid and a counter-clockwise boundary current that followed the tank perimeter. The Davies study emphasized the long-term evolution of the mixed layer after the boundary current had returned to the source. However, it also provided a qualitative picture of the horizontal distribution of the mixed fluid over the short time period before the boundary current reached the end of the tank and began its return, between five and thirty rotation periods after the onset of grid mixing. Davies *et al.* gave examples from two flow regimes: one with $N/f = 1.2$ and $L_C/L_R = 10$, and the other with $N/f = 4.8$ and $L_C/L_R = 2.5$. In the former, an electrolytically precipitated tracer showed a protrusion at the base of the boundary current that grew into a cyclonic eddy and merged with the mixed fluid in front of the grid. In the latter, the tracer simply showed the region of mixed fluid spreading out from the grid, while streak photography provided evidence of cyclonic circula-

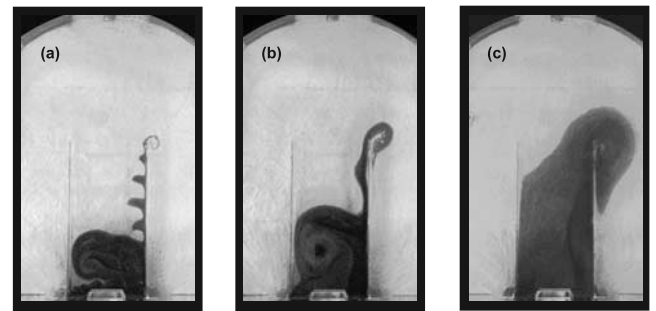


Figure 6. Dye images for three experiments with $\omega = 14 \text{ s}^{-1}$ and $L_C = 30.5 \text{ cm}$ at $t = 600 \text{ s}^{-1}$: (a) $(N, f) = (0.6, 1.2) \text{ s}^{-1}$, $N/f = \frac{1}{2}$, and $L_C/L_R = 15$; (b) $(N, f) = (0.6, 0.3) \text{ s}^{-1}$, $N/f = 2$, and $L_C/L_R = 3$; and (c) $(N, f) = (0.9, 0.1) \text{ s}^{-1}$, $N/f = 9$, and $L_C/L_R = 1$.

tion within the fluid. The images also showed the boundary current as a distinct structure, with a propagation speed that scaled with gravity current velocity and a width the order of the deformation radius. Overall, the early distribution of mixed fluid in the closed container prior to the return of the boundary current was similar to the developing flows observed in the open channel.

5. Quantitative Analysis and Scaling

[33] Quantitative analysis of the open channel experiments considers the extent of vertical mixing, the volume production of mixed fluid and its partition between the recirculation region and the boundary current. Vertical mixing is evaluated from measurements of the mixed layer height near the turbulent zone, but variations in layer height in the interior of the channel are treated separately for the recirculating cell and the boundary current. The volume of the recirculation region is calculated from area and height data collected from the time of its formation up to the development of instabilities or secondary cells. Data on boundary current length, height and area cover the period from the current's emergence to its arrival at the end of the channel.

5.1. Height of the Mixed Layer

[34] The height of the mixed layer was measured approximately four cm from the bar (see Figure 1). Turbulent overturning at the bar quickly established a mixed layer height that remained nearly steady throughout the experiments. A mean height h_m was calculated for each experiment from all measurements taken from $t = 300$ s until the side view was blocked by dye in the exterior basin. Figure 7 plots the mean height versus the buoyancy scale height, $\gamma (\frac{\omega}{N})^{1/2}$ (equation (10)), for fourteen experiments with $L_C = 30.5$ cm and $\omega = 14$ s $^{-1}$. The errorbars give the standard deviation about the mean height for the individual experiment. Only the larger values are visible. On average, the standard deviation is 5% of the mean value and the errorbar is smaller than the symbol size. A straight line fit with zero intercept gives

$$h_m = (0.93 \pm 0.06) \gamma \left(\frac{\omega}{N} \right)^{1/2}, \quad (16)$$

where $\gamma = 0.98$ cm is the experimentally determined constant related to the bar geometry and the turbulence model (from WH04). The constant 0.93 in equation (16) is only slightly less than that found in WH04 (equation (13)). Both unconfined and laterally confined mixing generate mixed layer heights proportional to the relative strength of imposed mixing and ambient stratification, and independent of rotation. Note that the WH04 experiments included variations in bar frequency with $\omega = [7, 14, 28]$ s $^{-1}$. The dependence of layer height on $\gamma(\frac{\omega}{N})^{1/2}$ is also consistent with the nonrotating grid-mixing experiments of *Ivey and Corcos* [1982], *Thorpe* [1982], and *Browand and Hopfinger* [1985].

[35] In the *Davies et al.* [1991] closed channel experiments, the mixed layer reached an initial equilibrium thickness that scaled with $(\frac{\omega}{N})^{1/2}$ and remained constant until the boundary current returned to the mixing region. Once the boundary current had circled the tank, mixed layer

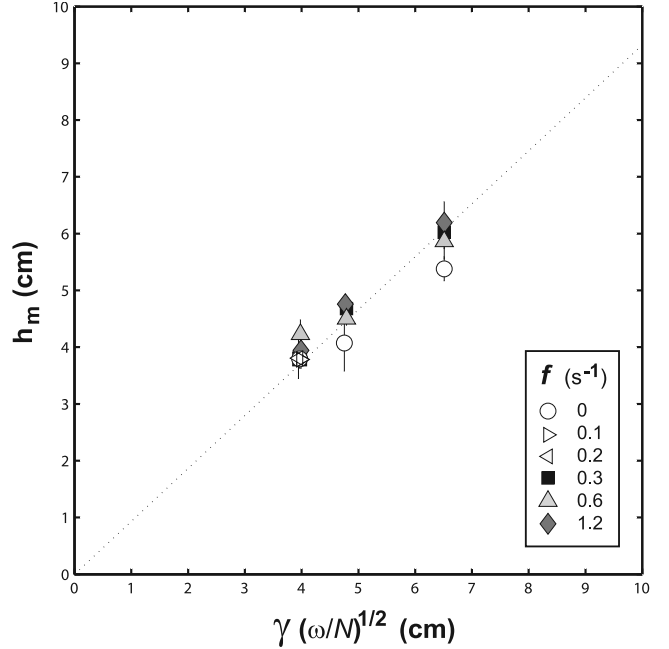


Figure 7. Mean height of mixed layer versus buoyancy scale height (equation (10)), for experiments with $\omega = 14$ s $^{-1}$, $0.3 \leq N \leq 0.9$ s $^{-1}$, $0 \leq f \leq 1.2$ s $^{-1}$, and $L_C = 30.5$ cm. Symbols indicate rotation rates for individual experiments.

growth resumed and thickness then became an increasing function of rotation. Davies et al. concluded that vertical entrainment was augmented over long times by the lateral injection of previously mixed fluid. This development is not observed in the present experiments since the boundary current exits the channel and does not return to the source. The mixed layer near the bar maintains a steady state height throughout the experiments and is unaffected by recirculation of mixed fluid in front of the bar.

5.2. Recirculation Region

[36] The volume of fluid in the recirculation region was calculated from measurements of the mixed layer height and the horizontal area of dyed fluid in front of the mixing bar. The plan view area measurements are shown in Figure 8 with area scaled by $L_C (L_R L_f)^{1/2}$ and timescaled by f^{-1} . The constant channel width L_C is included in the scaling for dimensional reasons and will be discussed in section 5.4. The area grows approximately as $t^{1/2}$, with $A_m \propto t^{0.59 \pm 0.14}$. The normalized area measurements are shown superimposed on the $(ft)^{1/2}$ curve. The data collapse quite well to

$$A_m = (0.32 \pm 0.04) L_C (L_R L_f)^{1/2} (ft)^{1/2}. \quad (17)$$

[37] In the WH04 experiments area growth was a function of $L_R L_f ft$ (equation (14)). Interestingly, equation (17) contains the square root of these same terms. The gradual blockage of the channel by mixed fluid offers a possible explanation for the new scaling. If mixed layer growth and lateral spreading initially followed the pattern of the unconfined experiments, the recirculating cell would expand with a radius, $r \sim (L_R L_f ft)^{1/2}$, and the open area along the left wall, $L_C - 2r$, would decrease with time. As this pathway

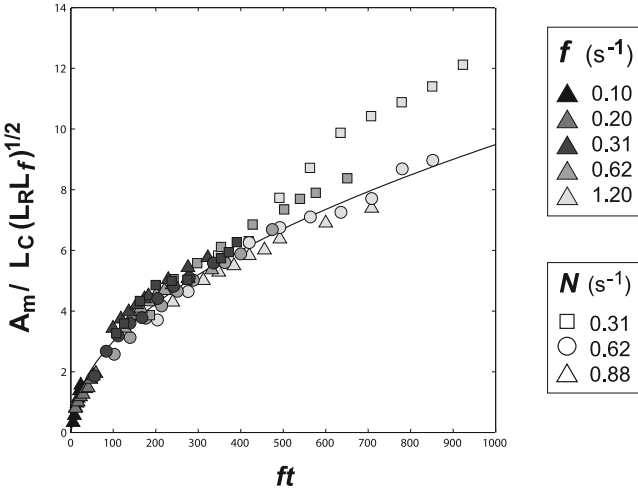


Figure 8. Horizontal area of mixed fluid for all rotating, stratified experiments with $L_C = 30.5$ cm. Symbols indicate values of N and f . Area is normalized by $L_C (L_R L_f)^{1/2}$ versus nondimensional time ft . L_R and L_f are given by equations (12) and (11), respectively.

between the basin exterior and the mixing zone was squeezed shut, the flux of ambient fluid toward the mixing zone would decrease. Consequently, the growth of the recirculation cell would be restricted.

[38] The mixed layer height measurements used in the volume calculations were adjusted for cross-channel variability. Side views of the recirculation region (see Figure 5b) give only the maximum cross-sectional heights. An estimate of height variability through the approximate center of the recirculation region was obtained from conductivity probe measurements taken along cross-channel transects 17 cm from the mixing bar.

[39] Figure 9 shows data from a transect of the channel taken at $t \approx 50$ min during an experiment with $(\omega, N, f) = (14, 0.33, 0.31)\text{s}^{-1}$ and $L_C/L_R = 4.7$. The seven vertical density profiles are staggered according to their cross-channel position from left to right, looking outward from the mixer. Profile spacing is closer across the boundary current. Each profile shows a nearly homogeneous layer located at middepth and separated from the linearly stratified fluid above and below it by sharp density interfaces. Together the profiles indicate a small but definite thinning of the mixed layer toward the center of the channel.

[40] The probe data was analyzed with the expectation that lateral variations in mixed layer height result from the cyclonic flow in the recirculation cell. The cell was modeled as a cylinder with antisymmetric cone-shaped upper and lower surfaces. Once mixed fluid had filled the channel, the slope of the cone was calculated for each transect from the maximum and mean heights of the homogeneous layer. A characteristic slope, $\Delta h / (\frac{1}{2}L_C)$, was then defined for the experiment.

[41] Ideally, an unconfined flow in geostrophic balance will show a change in height, $\Delta h \sim (f/N)l$, where l is the radius of the recirculating region. Here, over the range $\frac{1}{4} \leq N/f \leq 9$, the data give $\Delta h \sim (f/N)^{1/2} l$, with $l = \frac{1}{2}L_C$. This

gives a model of the mixed layer depth in the recirculation zone,

$$h_* = h_m - 0.03 \left(\frac{f}{N} \right)^{1/2} l(t), \quad (18)$$

where h_m is the mean mixed layer height measured near the turbulent zone. The second term is Δh as a function of time, where $l(t)$ is the half-length of the expanding recirculation region measured parallel to the mixing bar. Δh is weighted by a factor which incorporates the volumetric effects of the assumed cone geometry.

[42] The effect of using the adjusted height factor h_* is a reduction in calculated volumes that range from 3% to 11% of volumes calculated with uniform h_m . The reductions tend to increase with time and are greatest in those experiments with the lowest values of N/f . Had the structure of the recirculation region been based on a different model, with the slope occurring only in the region where the cell radius $\geq L_R$, the reduction in calculated volume would have been 2% to 5% greater. In either case, volume based on adjusted height scales the same as volume based on the mean height for each experiment. Figure 10a plots the normalized volume versus ft . Figure 10b presents the data in a loglog plot illustrating the $t^{1/2}$ behavior. The data give

$$V_m = (0.30 \pm 0.04)L_C (L_R L_f)^{1/2} h_m (ft)^{1/2}, \quad (19)$$

with h_m given by equation (16).

[43] The coefficient in equation (19) is derived from the best fit of the full data set to variations in N and f , but two

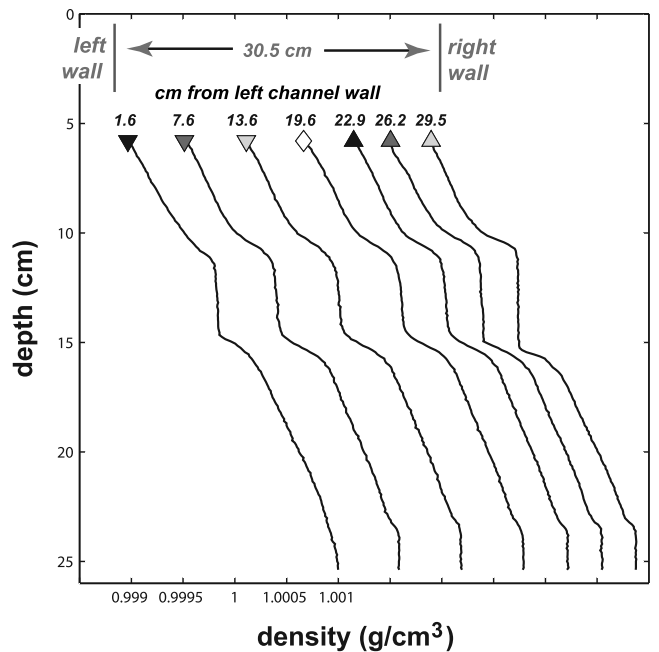


Figure 9. Density profiles for experiment with $(\omega, N, f) = (14, 0.3, 0.3) \text{s}^{-1}$ and $L_C = 30.5$ cm, taken 17 cm in front of the mixing bar at $t = 50$ min. $N/f = 1$ and $L_C/L_R = 4.7$. Profiles are staggered according to their spacing across the channel. The left-hand profile is pegged to the correct density.

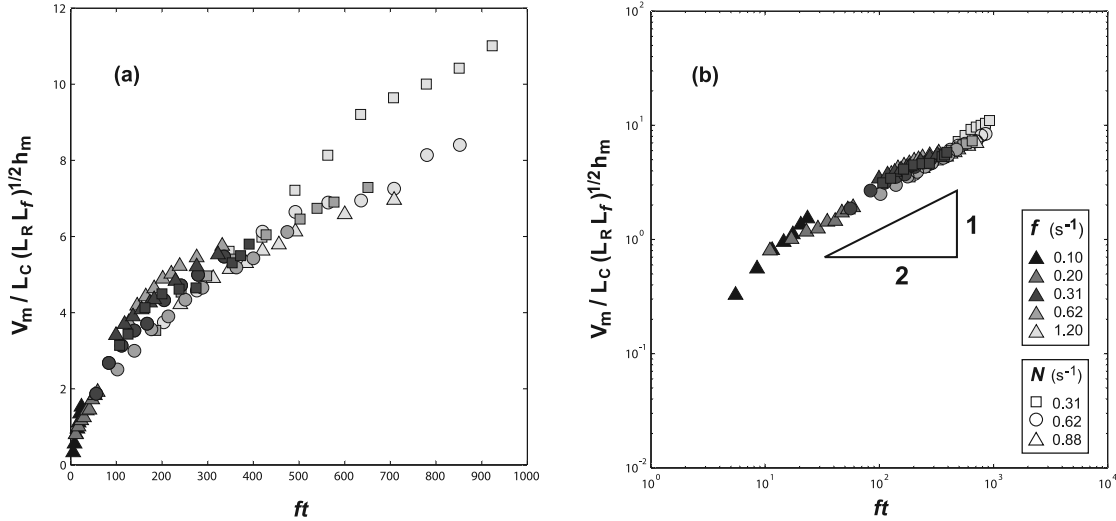


Figure 10. Volume of mixed fluid for all rotating, stratified experiments with $L_C = 30.5$ cm. Symbols indicate values of N and f . (a) Volume normalized by $L_C (L_R L_f)^{1/2} h_m$ versus nondimensional time ft . L_R , L_f , and h_m are given by equations (12), (11), and (16), respectively. (b) Same data in a loglog plot.

experiments, one at each end of the N/f parameter range, appear as outliers in Figure 10. The light gray squares ($N/f = \frac{1}{4}$ and $L_C/L_R = 18$), indicate rapid, sustained production of mixed fluid. The black triangles at the lower left of Figure 10b, show low initial volumes and a high growth rate for $N/f = 9$ and $L_C/L_R = 1$ (see Figure 6c).

5.3. Boundary Current

[44] The analysis above considers only the mixed fluid in front of the turbulent zone. However, the portion of the mixed fluid carried by the boundary current must be assessed to obtain a picture of total mixed fluid production. Moreover, the boundary current is the conduit for export of mixed fluid into the exterior basin.

[45] The advance of the boundary current was measured from the onset of mixing until the current left the channel. Figure 11 displays a loglog plot of boundary current length, normalized by the deformation radius L_R (equation (12)), versus nondimensional time ft . The boundary current advances approximately as $t^{3/4}$,

$$l_{bc} = (0.25 \pm 0.03)L_R(ft)^{0.76 \pm 0.14}. \quad (20)$$

The rate of advance of the boundary current nose,

$$\frac{dl_{bc}}{dt} = 0.19 N h_m (ft)^{-0.24}, \quad (21)$$

is proportional to $N h_m$, the speed of a gravity current with height h_m . The boundary current plan view area, A_{bc} , grows linearly in time (not shown). Deceleration of the current nose could be due to fluid entering the growing lateral lobes and sidewall viscous effects [Helfrich and Mullarney, 2005].

[46] A rough estimate of the volume of mixed fluid contained in the boundary current is obtained by noting that the boundary current depth on the wall varies parabolically from h_{bc} , the height of the boundary current measured where it emerges from the recirculation region (see Figure 5b), to zero at the nose. Both the layer thickness and the layer

width are also taken to vary parabolically. Thus the volume of the boundary current $V_{bc} = \frac{8}{15} h_{bc} A_{bc}$. The height h_{bc} remains relatively constant giving a linear growth in boundary current volume. Since the flux into the recirculation region decays with time, the boundary current carries an increasing percentage of the total mixed fluid. During the time period of the measurements, the maximum percentages are 1 to 4% for experiments with $N/f \leq 3$, and up to 14% for the experiments with $N/f = 4.5$ and $N/f = 9$. Overall, the boundary current volumes do not substantially change the previously determined relation for volume (equation (19)).

5.4. Variations in Channel Width

[47] In the WH04 unconfined experiments, mixed fluid production was independent of the mixing region width. In these confined experiments mixing region width, given by

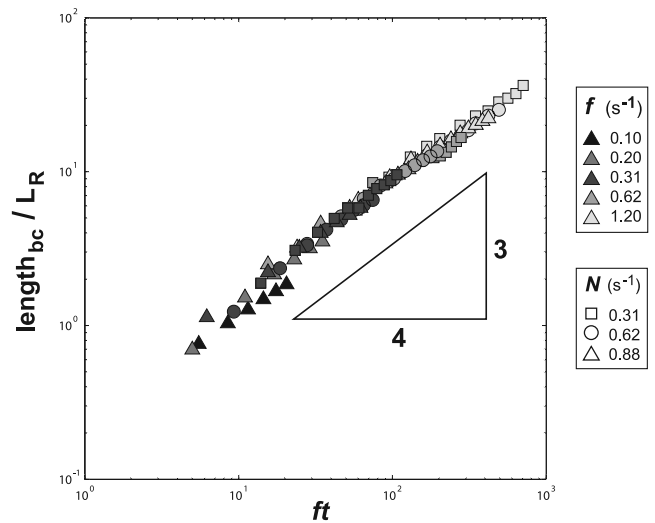


Figure 11. Advance of the boundary current for all rotating, stratified experiments with $L_C = 30.5$ cm. Symbols indicate values of N and f . Length is normalized by L_R (equation (12)) versus nondimensional time ft .

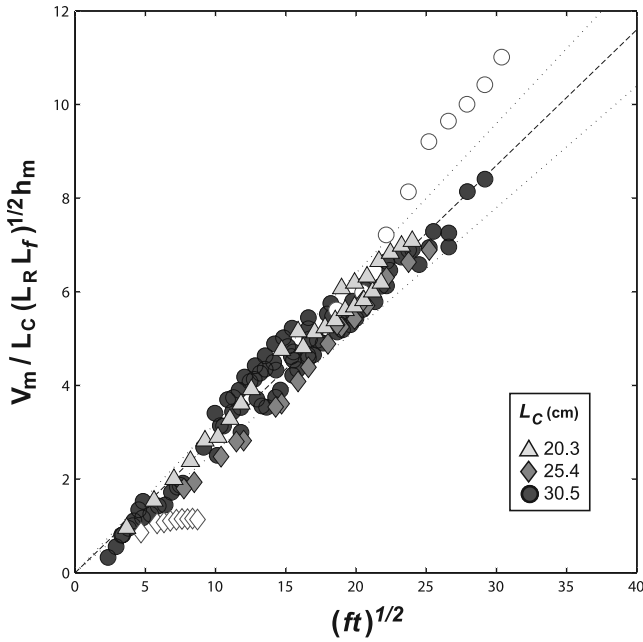


Figure 12. Volume of mixed fluid for all experiments. The symbols indicate the channel width L_C . Volume is normalized by $L_C (L_R L_f)^{1/2} h_m$ versus the square root of nondimensional time $(ft)^{1/2}$. L_R , L_f , and h_m are given by equations (12), (11), and (16), respectively.

the channel width L_C , is included in the scaling of mixed fluid volume for dimensional reasons, even though L_C is a constant 30.5 cm. The role of the channel width is examined in additional experiments with $L_C = [20.3, 25.4]$ cm. This variation is relatively small in part because of constraints imposed by the experimental apparatus. The results presented below apply within range investigated. For each channel width, three experiments were conducted with constant $N \approx 0.9 \text{ s}^{-1}$, and variable f , such that $0.7 \leq N/f \leq 4.5$ and $9.5 \geq L_C/L_R \geq 1.5$. The bar frequency was again fixed at $\omega = 14 \text{ s}^{-1}$. These experiments are marked on the regime diagram, Figure 2, by squares ($L_C = 20.3$ cm) and triangles ($L_C = 25.4$ cm).

[48] The additional experiments confirm that mixed layer heights are independent of channel width and given by equation (16). Boundary current properties conform to equations (20) and (21) and are not noticeably dependent on channel width. The partition of mixed fluid between the recirculation region and the boundary current also shows no significant change. The percentage of the total mixed fluid carried by the boundary current remains small during the measurement period and appears to be a function of N/f rather than L_C/L_R .

[49] The volume of mixed fluid in the recirculation region for all three channel widths is shown in Figure 12. Volume, normalized by $L_C (L_R L_f)^{1/2} h_m$, is plotted versus $(ft)^{1/2}$. This scaling gives the best fit to the data and is consistent with equation (19). Experiments conducted with $L_C = 25.4$ cm are on the low side, and one experiment, with $N/f = 4.5$, is anomalously low. Nevertheless, the overall collapse of the data indicates that the volume of mixed fluid in the recirculation region does indeed depend linearly on channel width.

The full data set gives $V_m = (0.29 \pm 0.05)L_C h_m (L_R L_f)^{1/2} (ft)^{1/2}$ with a correlation coefficient, $r = 0.97$. The volume of the recirculation region represents approximately 90% or more of the total production of mixed fluid. The flux of mixed fluid from the turbulent zone is a decreasing function of time,

$$Q = \frac{dV_m}{dt} = 0.15 L_C h_m (L_R L_f)^{1/2} f^{1/2} t^{-1/2}. \quad (22)$$

6. Geostrophic Transport Calculations

[50] The observed distributions of dyed fluid (section 4) describe a recirculation within the channel that appears to cut off lateral entrainment of unmixed fluid and curtail production of mixed fluid (equation (22)). However, the dye distributions mark only mixed fluid flows and are, moreover, difficult to quantify when instabilities and irregularities develop. The quantitative analysis thus covers a relatively short time period in the life of an experiment, generally less than 125 rotation periods. The series of vertical density profiles, described in section 5.2, cover the full duration of four experiments, and supplement the dye data with information about flows across a channel cross section at all depths, not just at the depth of the mixed layer.

[51] Repeated conductivity probe measurements were made along a transect through the approximate center of the recirculation region. The location of the transect is sketched in Figure 13, and a typical set of vertical density

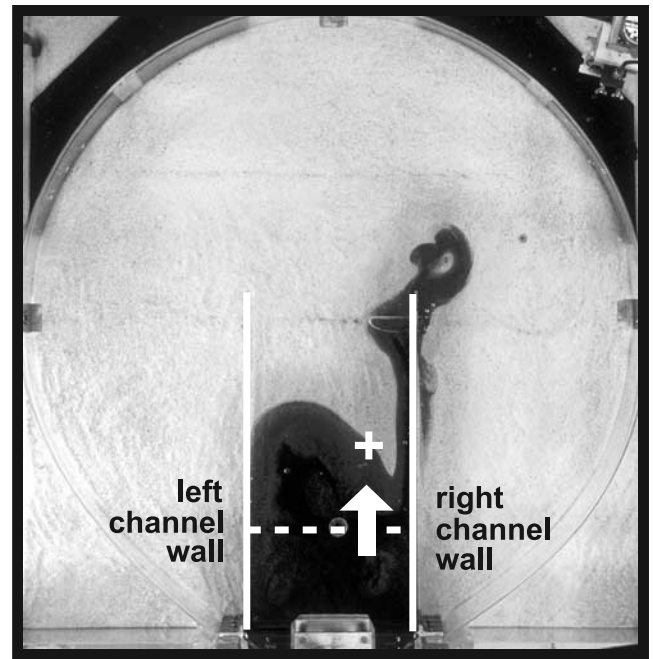


Figure 13. Diagram showing the location of the cross-channel probe transects (dotted line). White arrow indicates the direction of positive flow, away from the mixing bar. The diagram shows the dye image from the experiment with $(\omega, N, f) = (14, 0.3, 0.3) \text{ s}^{-1}$, $L_C = 30.5 \text{ cm}$, $N/f = 1$, and $L_C/L_R = 4.7$ at $t = 900 \text{ s}$.

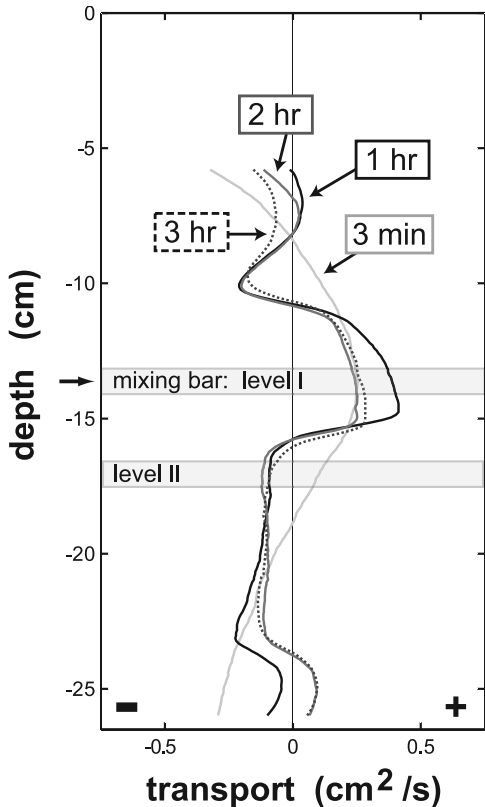


Figure 14. Horizontally integrated, along-channel volume transport ($\text{cm}^2 \text{s}^{-1}$) versus depth (cm) at the location shown in Figure 13. Positive values are down channel, away from the mixing bar. Geostrophic calculation is based on density data from the experiment with $(\omega, N, f) = (14, 0.3, 0.3) \text{ s}^{-1}$, $L_C = 30.5 \text{ cm}$, $N/f = 1$, and $L_C/L_R = 4.7$. The transport profiles are for four times as indicated, $t = [3 \text{ min}, 1 \text{ hour}, 2 \text{ hours}, 3 \text{ hours}]$. The shaded strips mark the location of the cross-channel details shown in Figure 15. Level I (see arrow) is centered at the depth of the mixing bar.

profiles is shown in Figure 9. The profiles extend from approximately six cm below the rigid lid to within one half cm of the sand bottom. Geostrophic velocities are calculated from the horizontal density differences between the profiles for four experiments with $N/f = [\frac{1}{4}, 1, 3, 9]$ and $L_C/L_R = [18, 4.7, 3, 1]$. To make the calculations, the flow outside the active mixing area is assumed to be in geostrophic balance. The observed flows were slow and laminar, and the Rossby numbers of the swiftest flows in the boundary current are of the order $O(10^{-2} \text{ to } 10^{-1})$. The level of no motion is taken to be at the base of the profiles. Finally, each transport calculation is adjusted to conserve volume. Density differences in the experiments are so small that conservation of mass does not provide an adequate additional constraint on the geostrophic calculation. Therefore net along-channel volume transport is set to zero by assigning a uniform barotropic velocity to the entire flow field.

[52] The examples of along-channel transport shown in Figures 14, 15, and 16 come from the experiment with $L_C = 30.5 \text{ cm}$, $(\omega, N, f) = (14, 0.33, 0.31) \text{ s}^{-1}$, $N/f = 1$ and $L_C/L_R = 4.7$. These are the same as the parameters of the

experiments pictured in Figures 9 and 13. Figure 14 shows four vertical profiles of the net horizontal along-channel volume transport per unit depth. The profiles show a net flow outward at the level of the mixed layer (the positive direction in the figures), and a net flow toward the mixing zone above and below the mixed layer. Figure 15 shows details of the horizontal flow structure, integrated vertically over one cm, at the two levels indicated in Figure 14. Level I is centered at the depth of the mixing bar. Level II is located below the mixed layer, at a depth of 17 cm.

[53] The geostrophic calculations indicate net outward flow within the boundary current and inward flow along the opposite wall. The four pairs of plots in Figure 15 display the volume transports through levels I and II for each of the four vertical profiles in Figure 14. At $t = 3 \text{ min}$, the boundary current is just crossing the transect and the flow is positive at both levels, though weaker below the mixed layer. At later times, $t = [1, 2, 3] \text{ hrs}$, the net flow at middepth is positive and concentrated near the right wall, while the net flow at the lower level is inward and concentrated along the left wall.

[54] Figure 16 plots the integrated along-channel transport in levels I and II for each of the eleven transects made over the course of the three hour experiment. The dark gray diamonds show the adjusted geostrophic calculations for transport at middepth. The transport at level I is superimposed on an estimate of the flux of mixed fluid from equation (22) for an equivalent one cm thick section. The geostrophic calculations with the uniform barotropic correction are consistent with the predictions derived from the dye observations. The data from the other three experiments are more scattered than that presented in Figure 16, but in all cases they show the recirculating flow strengthening over time and a net midlevel outflow declining with time. The flows imply that the export of fluid at the level of the mixed layer is being supplied in part by incoming unmixed fluid from the lower (and upper) levels. Hence vertical entrainment is a more important contributor to the flux of mixed fluid in the channel than in an unconfined environment (WH04).

[55] The boundary current export and the establishment of these inbound flows also implies that mixing within the channel influences stratification and circulation in the exterior basin. However, these effects are not measured in the present experiments.

7. Mixing in the Absence of Rotation: $f = 0$

[56] While local vertical mixing and the height of the mixed layer near the turbulent zone are found to be independent of rotation, the volume production of mixed fluid is a function of both rotation and stratification. For a given channel width L_C , stratification N , and bar frequency ω , decreasing the rotation rate f increases the production of mixed fluid. When equation (22) for volume flux is rewritten in terms of the external parameters, ω , N and f , using the formulae for h_m (equation (16)), L_R (equation (12)) and L_f (equation (11)), it becomes

$$Q \sim L_C \omega(Nf)^{-1/4} t^{-1/2}. \quad (23)$$

In the limit $f \rightarrow 0$, the predicted flux becomes infinite and a new scaling must occur. This issue is explored with four

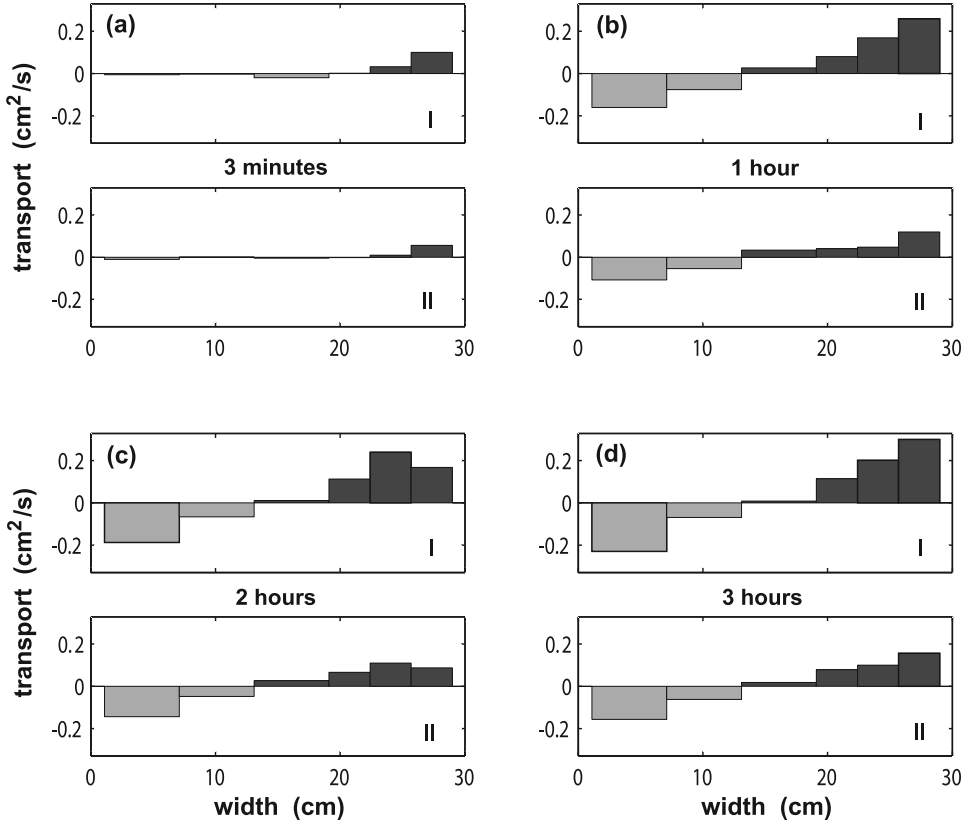


Figure 15. Vertically integrated, along-channel volume transport ($\text{cm}^2 \text{s}^{-1}$) versus channel width (cm) at the location shown in Figure 13: (a) $t = 3$ min, (b) $t = 1$ hour, (c) $t = 2$ hours, and (d) $t = 3$ hours. Vertical integrations are over 1 cm depths centered 13.75 and 17 cm below the rigid lid, levels I and II, respectively. Positive values are down channel, away from the mixing bar. Geostrophic calculation is based on density data from the experiment with $(\omega, N, f) = (14, 0.3, 0.3) \text{ s}^{-1}$, $L_C = 30.5 \text{ cm}$, $N/f = 1$, and $L_C/L_R = 4.7$.

stratified nonrotating experiments, three conducted using the original channel width, $L_C = 30.5 \text{ cm}$ and $N = [0.33, 0.62, 0.89] \text{ s}^{-1}$, and one with $L_C = 20.3 \text{ cm}$ and $N = 0.88 \text{ s}^{-1}$.

[57] The temporal mean mixed layer heights are designated by circular symbols in the plots in Figure 7. In three out of the four nonrotating experiments, the heights are on the low side, approximately 90% of the values predicted by the overall empirical relation for h_m (equation (16)). Note that, in the absence of rotation, the turbulent fluid collapses into a tapering intrusion. The heights, measured four cm in front of the mixing bar, would have been larger if measured closer to the turbulent zone.

[58] Volumes are estimated using the average height of the intrusion side view. Cross-channel layer height is assumed to be uniform. With these considerations, the volume scales with $h_m^3 Nt$ as shown in Figure 17. A linear fit to the data gives

$$V_m = (0.21 \pm 0.06) h_m^3 Nt. \quad (24)$$

In the nonrotating case, the volume of mixed fluid is independent of the channel width and production is constant.

$$\frac{dV_m}{dt} = Q = (0.21 \pm 0.06) N h_m^3. \quad (25)$$

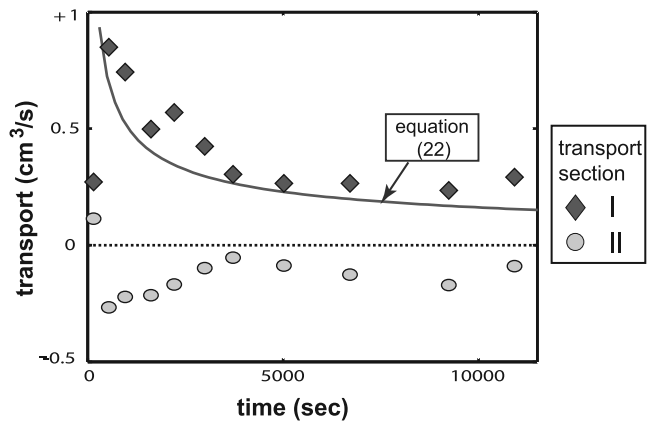


Figure 16. Along-channel volume transport ($\text{cm}^3 \text{s}^{-1}$) versus time (s) at the location shown in Figure 13. The transport is horizontally integrated across the channel and vertically integrated over 1 cm depths centered 13.75 and 17 cm below the rigid lid, levels I and II, respectively. Positive values are down channel, away from the mixing bar. Geostrophic calculations are based on density data from the experiment with $(\omega, N, f) = (14, 0.3, 0.3) \text{ s}^{-1}$, $L_C = 30.5 \text{ cm}$, $N/f = 1$, and $L_C/L_R = 4.7$. Solid curve is mixed fluid flux from equation (22).

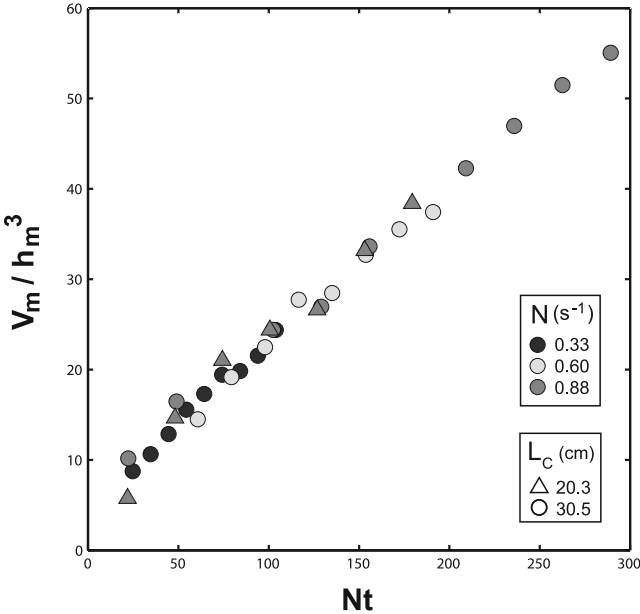


Figure 17. Volume of mixed fluid in experiments without rotation. Symbols indicate channel width and stratification. Volume is normalized by h_m^3 versus nondimensional time Nt .

The flux of mixed fluid (equation (25)) indicates a steady exchange flow proportional to Nh_m , scaled by the size of the maximum turbulent eddies h_m . Within the limited experimental range, $0.12 \leq h_m/L_C \leq 0.19$, the width of the mixing zone does not affect the production rate.

[59] Figure 18 compares the dimensional mixed fluid volume growth for four experiments with and without rotation. The experiments have the same channel width, bar frequency and stratification, $L_C = 30.5$ cm, and $(\omega, N) = (14, 0.6) \text{ s}^{-1}$, but different rotation rates, $f = [0, 0.3, 0.6, 1.2] \text{ s}^{-1}$. These observations are superimposed on the growth curves predicted by the empirical scalings (equations (19) and (24)). The results clearly demonstrate the restrictive effect of rotation on the production of mixed fluid.

8. Discussion

[60] A comparison of the volume production of mixed fluid due to unconfined vertical boundary mixing (WH04) and confined channel mixing is shown in Figure 19. Measured and predicted volumes are shown for four experiments, two each for unconfined and confined mixing, with $f = 0$ and $f = 0.3 \text{ s}^{-1}$. The bar and buoyancy frequencies are the same in all four, $(\omega, N) = (14, 0.3) \text{ s}^{-1}$, as is the width of the mixing region, $(L_C, L_B) = 30.5$ cm. The presence of the channel walls reduces production of mixed fluid in both rotating and nonrotating experiments, and the rotating experiments are further distinguished by the $t^{-1/2}$ time dependence of mixed fluid flux (equation (22)). In the rotating case, the channel walls not only eliminate direct access to the sides of the mixing region, they also promote the formation of a boundary current and a recirculation region in front of the mixing bar. As the recirculating cell spreads across the channel it restricts the inflow of stratified fluid to the mixing region. Moreover, mixed fluid within the recirculating cell is trapped within the channel.

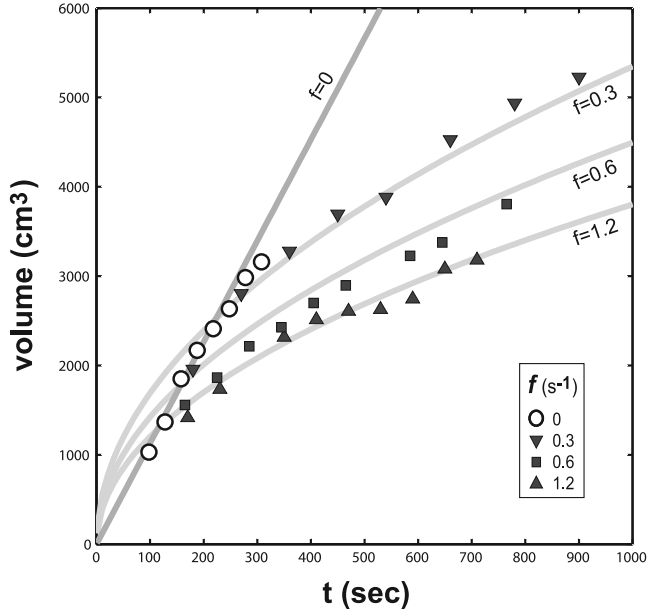


Figure 18. Volume of mixed fluid in experiments with and without rotation. Volume (cm^3) versus time (s). All experiments have $(\omega, N) = (14, 0.6) \text{ s}^{-1}$ and $L_C = 30.5$ cm. The solid lines are volume growth predicted by the empirically derived equations (19) and (24). The symbols are data points from the experiments with $f = [0, 0.3, 0.6, 1.2] \text{ s}^{-1}$.

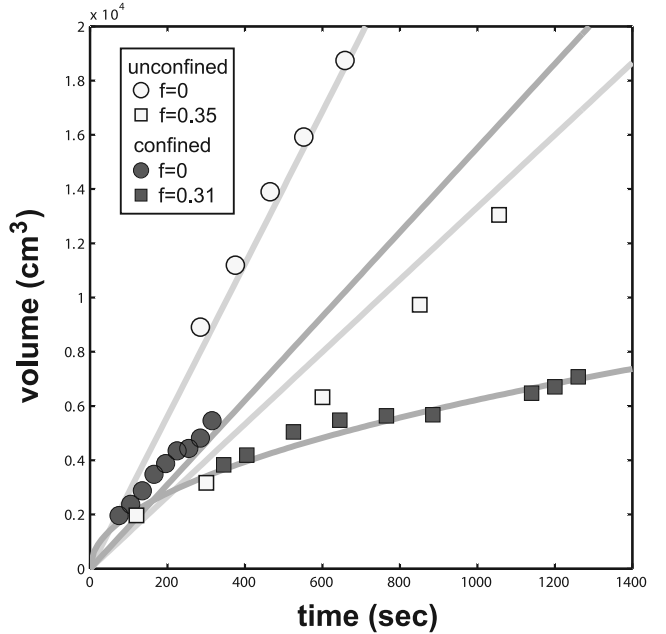


Figure 19. Volume of mixed fluid in unconfined (WH04) and laterally confined experiments with $f = [0, 0.3] \text{ s}^{-1}$ showing volume (cm^3) versus time (s). All experiments have $(\omega, N) = (14, 0.3) \text{ s}^{-1}$ and $L_B, L_C = 30.5$ cm. From left to right, the solid lines are volume growth predicted by empirically derived equations (WH04, equation (32); WH04, equation (24); equation (24); and equation (19), respectively). The symbols are data points from individual experiments. Note that the rotation period for one cycle is 42 s.

Table 1. Typical Values of the Buoyancy Frequency N and the Dissipation Rate of Turbulent Kinetic Energy ε for Five Sites^a

Site	Depth, m	L_C , km	N , s ⁻¹	f , s ⁻¹	ε , m ² s ⁻³	N/f
N. C. shelfbreak canyon	1,100	2 ± 0.5	1×10^{-3}	8.7×10^{-5}	6×10^{-9}	11
Monterey canyon (<i>LOa</i>)	400	1.5 ± 0.5	3.3×10^{-3}	8.7×10^{-5}	8.7×10^{-8}	38
Monterey canyon (<i>LOB</i>)	525	1.5 ± 0.5	8.8×10^{-3}	8.7×10^{-5}	5.1×10^{-7}	100
Monterey canyon (<i>CG</i>)	250	1.5 ± 0.5	8.2×10^{-3}	8.7×10^{-5}	1.1×10^{-6}	94
MidAtlantic Ridge canyon	4,550	16 ± 3	7.7×10^{-4}	5.4×10^{-5}	2×10^{-9}	14

^aAlso listed are canyon width L_C , Coriolis frequency f , and N/f .

[61] Note, however, that these findings are based on measurements made prior to the development of instabilities on the cell rim and the boundary current (see section 4.2 and Figures 4, 5, and 6). The experiments have not considered the effects of wave-like disturbances and eddies on the transport of mixed fluid into the channel interior, or the exterior basin. Nor have the experiments considered the fate of the recirculating fluid once mixing ceases. *Nof* [1988] demonstrated that isolated eddies will leak fluid when they come into contact with a wall. It is possible that the recirculating fluid within the channel will drain into the boundary current until the cell has shrunk to a size that barely touches the walls. The boundary current, which serves as the sole conduit for mixed fluid entering the exterior basin, may ultimately transport much of the mixed fluid out of the channel. Another interesting question is what happens in sustained mixing when the mixed fluid occupies the full length of the channel. It is possible that instabilities and eddy shedding along the front at the channel opening could then dominate the mixed fluid transport into the basin.

[62] In order to examine the applicability of the experimental observations to oceanic mixing, the laboratory length scales have been rewritten in terms of the dissipation rate of turbulent kinetic energy $\varepsilon = u_t^3/l$ (equation (7)), using the relationship between the mixed layer height h_m (equation (13)) and the Ozmidov scale $L_O = (\varepsilon/N^3)^{1/2}$ (equation (6)). Previous laboratory studies [*Thorpe*, 1982; *Browand and Hopfinger*, 1985; *Davies et al.*, 1991; *De Silva and Fernando*, 1998] found values between 1 and 5 for the ratio of critical height to Ozmidov length. A similar relationship was also established in an observational study of wind-driven mixing [*Dillon*, 1982]. Dillon calculated vertical overturning scales, L_T , from density profiles [*Thorpe*, 1977] and found them to be directly proportional to the Ozmidov scale, $L_T/L_O \approx 1.25$. The channel experiments showed $h_m/L_O \approx 4$, giving

$$h_m \approx 4 \left(\frac{\varepsilon}{N^3} \right)^{1/2}. \quad (26)$$

With appropriate substitutions in the formulae for L_R (equation (12)) and L_f (equation (11)), the length scales are defined as functions of N , f and ε .

$$L_R \approx 4 \left(\frac{N}{f} \right) \left(\frac{\varepsilon}{N^3} \right)^{1/2} \quad (27)$$

$$L_f \approx 4 \left(\frac{N}{f} \right)^{1/2} \left(\frac{\varepsilon}{N^3} \right)^{1/2}. \quad (28)$$

[63] The implications for oceanic mixing are examined on the basis of five sets observations: one from a shelfbreak canyon off North Carolina [*Montgomery and Polzin*, 1999], three from Monterey Canyon off California denoted in the tables as *LOa*, *LOB* [*Lueck and Osborn*, 1985] and *CG* [*Carter and Gregg*, 2002], and one from a MidAtlantic Ridge fracture zone in the Brazil Basin [*St. Laurent et al.*, 2001]. Table 1 shows typical values of N and ε for a representative depth at each site. It also gives f , N/f and L_C . Canyon widths at the observation depths are roughly estimated from topographic maps, $1.5 \leq L_C \leq 16$ km.

[64] Table 2 shows estimates for length scales h_m (equation (26)), L_R (equation (27)) and L_f (equation (28)) based on the field data. The coefficient in equation (26), which is determined from laboratory measurements, produces reasonable estimates for observed mixed layer heights of $3.5 \text{ m} \leq h_m < 10 \text{ m}$. The calculated heights for Monterey Canyon compare well with the *Lueck and Osborn* [1985] observations of 2 to 5 m thick turbulent mixed layers.

[65] These estimates for L_R and L_f are for individual layers of height h_m . It is possible that the scales depend also on the overall height of the dissipation region. Experimental studies [*Ivey and Corcos*, 1982; *Thorpe*, 1982; and *Browand and Hopfinger*, 1985] have shown that turbulent mixing over an extended vertical distance produces multiple layers of mixed fluid. If stacked layers of mixed fluid, exported from the regions of intense dissipation, acted as a single vertically coherent unit with respect to the ambient stratification and rotation, both the volume and horizontal distribution of mixed fluid would increase. The question of the collective behavior of a number of vertically stacked intrusions in the presence of rotation was not investigated, but it could readily be explored in a future study.

[66] The values of N/f achievable in the laboratory, $\frac{1}{4} \leq N/f < 10$, are 2 orders of magnitude less than the field values, $10 < N/f \leq 100$. While the experiments show the recirculation cell remaining within the channel, as $N/f \rightarrow O(10)$ the percentage of mixed fluid carried by the boundary current

Table 2. Calculated Values for Mixed Layer Height h_m (Equation (26)), Deformation Radius L_R (Equation (27)), Rotational Length Scale L_f (Equation (28)), the Ratio of Canyon Width to Deformation Radius L_C/L_R , and Theoretical Time Required for a Recirculation Cell to Block the Canyon T_B (Equation (29))

Site	h_m , m	L_R , m	L_f , m	L_C/L_R	T_B , days
N. C. shelfbreak canyon	9.8	108	33	19.0 ± 4.6	9×10^2
Monterey canyon (<i>LOa</i>)	6.2	236	38	6.4 ± 2.0	2×10^2
Monterey canyon (<i>LOB</i>)	3.5	350	35	4.2 ± 1.4	1.5×10^2
Monterey canyon (<i>CG</i>)	5.6	526	54	2.9 ± 1.0	6×10^1
MidAtlantic Ridge canyon	8.4	118	31	136 ± 25	9×10^4

jumps from $\sim 1\text{--}3\%$ to more than 10%. Thus the experimental results may underpredict the actual export of canyon-mixed water into the open ocean via the boundary current.

[67] The experimental range, $1 \leq L_C/L_R \leq 18$, is representative of conditions for shelfbreak canyons, $2.9 \leq L_C/L_R \leq 19$, but not for the abyssal fracture zone where $L_C/L_R = 136$. Application of experimental results to the latter case is very tentative. In all the laboratory experiments the channel eventually becomes choked by the cyclonic recirculation cell. However, this is the result of sustained mixing and does not take into account the intermittent nature of oceanic turbulence. The following calculation makes an idealized estimate of T_B , the time required for the recirculation cell to fully span the channel. Assuming a circular recirculation cell with diameter, $2r = 2(A_m/\pi)^{1/2}$, where A_m is the horizontal area (equation (17)), the canyon width L_C would be blocked when $2r = 2((.32/\pi)L_C(L_RL_f ft)^{1/2})^{1/2} = L_C$. Solving for t gives the blocking time T_B

$$T_B = 6(L_C)^2 / (L_R L_f f). \quad (29)$$

[68] The values of T_B , listed in Table 2, range from 60 to 900 days for the shelfbreak canyons (and almost 250 years for the abyssal fracture zone). Observations in Monterey Canyon [Carter and Gregg, 2002], which show turbulent intensities varying over timescales of 15 to 30 days, indicate that canyon size recirculations are unlikely. However, the laboratory experiments have shown that mixing at the head of a channel in the presence of rotation generates a recirculation cell that, even in its early stages, restricts mixed fluid production and traps mixed fluid within the channel. The important lesson from the experiments is that rough topographic features that promote turbulent mixing can also limit the production and influence the distribution of mixed fluid.

[69] **Acknowledgments.** This work was supported by the Ocean Ventures Fund, the Westcott Fund, and the WHOI Academic Programs Office. Financial support was also provided by the National Science Foundation through grant OCE-9616949.

References

- Browand, F. K., and E. J. Hopfinger (1985), The inhibition of vertical turbulent scale by stable stratification, in *Turbulence and Diffusion in Stable Environments*, edited by J. C. R. Hunt, pp. 15–27, Oxford Univ. Press, New York.
- Carter, G. S., and M. C. Gregg (2002), Intense, variable mixing near the head of Monterey Submarine Canyon, *J. Phys. Oceanogr.*, **32**, 3145–3165.
- Davies, P. A., H. J. S. Fernando, P. Besley, and R. J. Simpson (1991), Generation and spreading of a turbulent mixed layer in a rotating, stratified fluid, *J. Geophys. Res.*, **96**, 12,567–12,585.
- De Silva, I. P. D., and H. J. S. Fernando (1998), Experiments on collapsing turbulent regions in stratified fluids, *J. Fluid Mech.*, **358**, 29–60.
- Dickinson, S. C., and R. R. Long (1983), Oscillating-grid turbulence including effects of rotation, *J. Fluid Mech.*, **126**, 315–333.
- Dillon, T. M. (1982), Vertical overturns: A comparison of Thorpe and Ozmidov length scales, *J. Geophys. Res.*, **87**, 9601–9613.
- Fernando, H. J. S. (1988), The growth of a turbulent patch in a stratified fluid, *J. Fluid Mech.*, **190**, 55–70.
- Fleury, M., M. Mory, E. J. Hopfinger, and D. Auchere (1991), Effects of rotation on turbulent mixing across a density interface, *J. Fluid Mech.*, **223**, 165–191.
- Gardner, W. D. (1989), Periodic resuspension in Baltimore canyon by focusing of internal waves, *J. Geophys. Res.*, **94**, 18,185–18,194.
- Griffiths, R. W. (1986), Gravity currents in rotating systems, *Annu. Rev. Fluid Mech.*, **18**, 59–89.
- Griffiths, R. W., and P. F. Linden (1982), Laboratory experiments on fronts. part I: Density-driven boundary currents, *Geophys. Astrophys. Fluid Dyn.*, **19**, 159–187.
- Helffrich, K. R., and J. C. Mullaney (2005), Gravity currents from a dam-break in a rotating channel, *J. Fluid Mech.*, **536**, 253–283.
- Hickey, B. M. (1995), Coastal submarine canyons, in *Topographical Effects in the Ocean: Proceedings of “Aha Huliko,” a Hawaiian Winter Workshop*, edited by P. Müller and D. Henderson, pp. 95–110, Univ. of Hawaii at Manoa, Honolulu.
- Hopfinger, E. J., and J.-A. Toly (1976), Spatially decaying turbulence and its relation to mixing across density interfaces, *J. Fluid Mech.*, **78**, 155–175.
- Hopfinger, E. J., F. K. Browand, and Y. Gagne (1982), Turbulence and waves in a rotating tank, *J. Fluid Mech.*, **125**, 505–534.
- Hunkins, K. (1988), Mean and tidal currents in Baltimore Canyon, *J. Geophys. Res.*, **93**, 6917–6929.
- Ivey, G. N., and G. M. Corcos (1982), Boundary mixing in a stratified fluid, *J. Fluid Mech.*, **121**, 1–26.
- Kunze, E., L. K. Rosenfeld, G. S. Carter, and M. C. Gregg (2002), Internal waves in Monterey Canyon, *J. Phys. Oceanogr.*, **32**, 1890–1913.
- Ledwell, J. R., E. T. Montgomery, K. L. Polzin, L. C. St.Laurent, R. W. Schmitt, and J. M. Toole (2000), Evidence for enhanced mixing over rough topography in the abyssal ocean, *Nature*, **403**, 179–182.
- Linden, P. F. (1973), The interaction of a vortex ring in a sharp density interface: A model for turbulent entrainment, *J. Fluid Mech.*, **60**, 467–480.
- Lueck, R. G., and T. R. Osborn (1985), Turbulence measurements in a submarine canyon, *Cont. Shelf Res.*, **4**, 681–698.
- Montgomery, E. T., and K. L. Polzin (1999), Turbulence and waves over irregularly sloping topography: Cruise report—Oceanus 324, *Tech. Rep. WHOI-99-16*, 42 pp., Woods Hole Oceanogr. Inst., Woods Hole, Mass.
- Munk, W., and C. Wunsch (1998), Abyssal recipes II: Energetics of tidal and wind mixing, *Deep Sea Res., Part I*, **45**, 1977–2010.
- Nof, D. (1988), Draining vortices, *Geophys. Astrophys. Fluid Dyn.*, **42**, 187–208.
- Oster, G. (1965), Density gradients, *Sci. Am.*, **213**, 70–76.
- Ozmidov, R. V. (1965), On the turbulent exchange in a stably stratified ocean, *Izv. Atmos. Oceanic Phys., Engl. Transl.*, **1**, 493–497.
- Polzin, K. L., J. M. Toole, J. R. Ledwell, and R. W. Schmitt (1997), Spatial variability of turbulent mixing in the abyssal ocean, *Science*, **276**, 93–96.
- St. Laurent, L. C., J. M. Toole, and R. W. Schmitt (2001), Buoyancy forcing by turbulence above rough topography in the abyssal Brazil Basin, *J. Phys. Oceanogr.*, **31**, 3476–3495.
- Thorpe, S. A. (1977), Turbulence and mixing in a Scottish loch, *Philos. Trans. R. Soc. London, Ser. A*, **286**, 125–181.
- Thorpe, S. A. (1982), On the layers produced by rapidly oscillating a vertical grid in a uniformly stratified fluid, *J. Fluid Mech.*, **124**, 391–409.
- Turner, J. S. (1973), Mixing across density interfaces, in *Buoyancy Effects in Fluids*, pp. 288–312, Cambridge Univ. Press, New York.
- Wells, J. R., and K. R. Helffrich (2004), A laboratory study of localized mixing in a rotating stratified fluid, *J. Fluid Mech.*, **516**, 83–113.

K. R. Helffrich, Woods Hole Oceanographic Institution, Woods Hole, MA 02543, USA.

J. R. Wells, Department of Ocean and Resources Engineering, University of Hawaii at Manoa, Honolulu, HI 96822, USA. (wellsjr@hawaii.edu)